Empirical selection of Auroral Kilometric Radiation during a multipoint remote observation with Wind and Cassini

J. E. Waters[1], C. M. Jackman[2], D. K. Whiter[1], X. Bonnin[3], B. Cecconi[3], L. Lamy[3], K. Issautier[3]

[1]Space Environment Physics Group, School of Physics and Astronomy, University of Southampton, Southampton, UK
[2]School of Cosmic Physics, DIAS Dunsink Observatory, Dublin Institute for Advanced Studies, Dublin 15, Ireland
[3]LESIA, Observatoire de Paris, PSL Research University, CNRS, Sorbonne Université, Univ. Paris, Meudon, France

Key Points:

- Novel, empirically-based method to extract AKR from Wind/WAVES is presented and applied to observations made during the Cassini flyby
- Selected data shows a distribution of AKR power with expected longitudinal visibility constraints
- Diurnal temporal modulation observed in selected data, showing agreement with multiple AKR observations with other spacecraft

Corresponding author: James Waters, J.Waters@soton.ac.uk

Abstract

Auroral Kilometric Radiation (AKR) is radio emission that originates in particle acceleration regions along magnetic field lines, coinciding with discrete auroral arcs. Found in both hemispheres, an increase in the amplitude of a particular AKR source denotes the strengthening of parallel electric fields in the auroral zone, while the emission frequency gives insight into source region morphology. AKR viewing geometry is complex due to the confinement of the source regions to nightside local times and the anisotropy of the beaming pattern, so observations are highly dependent on spacecraft viewing position. We present a novel, empirical technique that selects AKR emission from remote radio observations made with the spin-axis aligned antenna of the Wind/WAVES instrument, based on the rapidly varying amplitude of AKR across spacecraft spin timescales. This selection is applied to 30 days of data in 1999, during which the Cassini spacecraft flew close to Earth and recorded AKR for the majority of the period, while the Wind spacecraft completed close to two, precessing petal orbits. We examine the flux density and integrated power, which gives an occurrence distribution with spacecraft local time that is typical of AKR, with an increase in power of around 10^3 Wsr^{-1} between dayside and nightside observations. We also find a statistically significant ($p < 10^{-5}$), previously observed diurnal modulation of the AKR integrated power for the period, further verifying the empirical selection of AKR and showing the promise of its application to larger subsets of Wind/WAVES observations.

Plain Language Summary

Auroral Kilometric Radiation (AKR) is naturally occuring radio emission that is generated along magnetic field lines at high latitudes, and is coincident with brightenings of the aurora and other processes in the magnetosphere. In this work, we present a novel selection of AKR emission by quantifying the variability of the radio measurements during a frequency sample made by the Wind spacecraft. This technique is applied to 30 days of observations from the Wind spacecraft to compare with AKR emission observed by the Cassini spacecraft as it flew by Earth with a much different trajectory. Typical characteristics of AKR are observed with the selection from Wind, with the temporal modulation of emitted AKR power, as well as its distribution with spacecraft longitude, agreeing with previous observations. Namely, we see an increase of 10^3 Wsr^{-1} between selected Wind observations made on the nightside over those on the dayside as well as a statistically significant diurnal periodicity. These results verify the selection of AKR described here and show promise for future application with Wind.

1 Introduction

Auroral kilometric radiation (AKR) describes amplified radio emission from the Earth that has interacted with relativistic, upgoing electrons along magnetic field lines in the auroral zone, and resonates at the electron cyclotron frequency (C. S. Wu & Lee, 1979). The emission frequency of an AKR source is close to the local electron gyrofrequency, so that lower frequency AKR emanates from a higher altitude along a field line. AKR is emitted between $\sim 30-800$ kHz and has been observed by many Earth-orbiting spacecraft such as Polar, Geotail and Cluster (e.g., Liou et al., 2000; Mutel et al., 2003; Anderson et al., 2005; Morioka et al., 2007). The emission mechanism, the electron cyclotron maser instability, is such that AKR is emitted at angles near-perpendicular to the field lines. This leads to largely anisotropic beaming of AKR from individual field lines that has been constrained both through modelling and observations. Earliest observations suggested that AKR can be observed within a cone at angles that are increasingly oblique to the magnetic field with decreasing frequency (Green et al., 1977; Kasaba et al., 1997). However, more recent observations using Cluster suggests that AKR is emitted in a more restricted geometry, with similar longitudinal extent up to a few thousand

km but emitted over a narrower latitudinal region of a few tens of degrees over the auroral zone (Mutel et al., 2008).

Furthermore, AKR is known to be fully circularly polarised, with the handedness depending on the direction of electron gyration in either hemisphere (Kaiser et al., 1978). Where polarisation information is available, we expect to see left-handed circularly polarised (LH) emission from the Southern magnetic hemisphere and right-handed circularly polarised (RH) emission from the Northern magnetic hemisphere (assuming emission in the extraordinary mode). This has been observed at both Earth and Saturn and is a consequence of the emission mechanism (Lamy, Zarka, Cecconi, Prangé, et al., 2008; Lamy et al., 2010). The visibility of AKR is a strong function of the position of the observer. AKR and its source regions are mostly concentrated at nightside local times; AKR has been observed consistently from local times between ∼1600-0300 LT, whereas the most intense source regions are located at 2100-2200 LT (e.g., Gurnett, 1974; Alexander & Kaiser, 1976; Panchenko, 2003). The visibility of AKR to a spacecraft at various latitudes is constrained by the beaming of the emission, as mentioned above. Ray tracing has been used previously to examine the general propagation of AKR from the source region as well as for instances where the emission may refract; from the dense plasmasphere, for example (Green et al., 1977; Mutel et al., 2004). AKR visibility with latitude has also been examined statistically for studies of hemispheric conjugacy using multiple spacecraft (Morioka et al., 2011). For a spacecraft near the equator, it is possible to observe AKR emission from both hemispheres as the emission cones from sources on a given meridian overlap. In this case the emission from each pole cannot be separated (without polarisation information) and the observations must be interpreted as a global average. For closer radial distances a spacecraft near the equator can be beneath the superposed emission cones of each hemisphere and observe no AKR. At Saturn, this equatorial shadow zone has been modelled and found at radial distances of $< 3.6R_s$, where $R_S = 60268$ km is the radius of Saturn (Lamy, Zarka, Cecconi, Hess, & Prangé, 2008). At Earth, Morioka et al. (2011) attributed an approximate limit of $7R_E$ to the equatorial shadow zone, where $R_E = 6371$ km is the radius of Earth.

Given that AKR generation is intrinsic to the magnetic field, the tilt of the planetary field with respect to the rotation axis combines with the highly directive AKR beaming to produce an illumination region that is time-dependent. Temporally, significant periodicities have been found at semi-diurnal and diurnal timescales, the latter of which has been attributed to geometrical viewing effects as the emission region precesses, like the magnetic dipole, with respect to the rotation of the Earth (Lamy et al., 2010). Other suggestions for the source of this modulation include an intrinsic modulation due to the effect on the ionosphere of the tilt of the magnetic dipole with respect to the incoming solar wind (Panchenko et al., 2009) or a physical origin within the magnetosphere itself (Morioka et al., 2013). Discerning the origin of this variability is useful to further the understanding of the magnetosphere-ionosphere coupling.

In this paper we are concerned with the extraction of AKR from the raw data of an Earth-orbiting spacecraft, as well as the interpretation and quantification of any visibility effects due to the location of the spacecraft relative to the radio sources. Moreover, the AKR has the potential to serve as an excellent diagnostic tool both for solar wind driving and for magnetospheric dynamics. Specifically, previous work has shown that AKR can intensify during periods of magnetospheric disturbance (Voots et al., 1977; Liou et al., 2000; Zhao et al., 2019). The generation of AKR requires the presence of strong, parallel electric fields that accelerate electrons to the necessary relativistic speeds within the magnetosphere-ionosphere coupling region. The well-studied physical phenomenon of the magnetospheric substorm manifests in various observable signatures in both the magnetosphere and ionosphere. In the magnetosphere, the magnetic field dipolarises following reconnection in the magnetotail and energetic plasma flows Earthward (Liou, 2002; Juusola et al., 2011). Energetic particles are injected into the ionosphere as the substorm

current wedge strengthens the current systems at high latitudes, brightening the aurora and causing well known morphological changes in the oval (Akasofu, 1964; McPherron et al., 1973; Kepko et al., 2015). For AKR, not only does the emission intensify but the frequency spectrum undergoes characteristic changes in response to substorm behaviour. Observations with the Polar spacecraft have shown that the AKR source region morphology may have a dual structure, suggesting that a given field line has a more persistent AKR source at lower altitudes that suddenly extends to higher altitudes at the time of substorm onset (Morioka et al., 2007).

Before the properties of AKR can be studied in detail, the AKR-related radio signals must be disentangled from other radio emissions detected by a spacecraft radio instrument. This non-trivial process is described in more detail in Section 2 below. Broadly speaking, an orbiting spacecraft, when surveying the radio environment may detect multiple possible sources of radio emission at multiple wavelengths. At kilometric wavelengths, corresponding to frequencies of ~ 1 MHz and below, the long, drifting tails of solar radio type III bursts can be observed, which are ubiquitous when the spacecraft is in the solar wind (Krupar et al., 2018). As well as this, characteristic frequencies of the local plasma can be observed at lower frequencies. This can occur both in the solar wind, at the plasma frequency and harmonics following Langmuir waves, or within the magnetosphere, where dense, turbulent plasma in the magnetosheath leads to a rise in quasi-thermal noise (QTN) (Meyer-Vernet et al., n.d.; Meyer-Vernet et al., 2017). Thus AKR is often observed in superposition with other waves and must be explicitly selected, where possible, for a complete study. Goniopolarimetric (GP) inversion techniques are useful for selecting AKR, as the Stokes parameters of an incident wave can be derived using a model that accounts for the geometry of both the radio antennae and the source (Cecconi, 2019). Then, the circular polarisation can be used to discriminate against other sources; the few observations of solar radio Type III bursts at frequencies < 1 MHz show weak polarisation (Reiner et al., 2007; Pulupa et al., 2019). This has been done at Saturn, using the radio instrument on board the three-axis stabilised Cassini to observe SKR, the Kronian analog of AKR. As the Cassini spacecraft flew by Earth, its radio instrument was turned on for a month long period. During this time, the instrument was used to retrieve the circular polarisation state of the AKR, allowing the general emission characteristics, such as the emission power, and the temporal modulation to be studied (Lamy et al., 2010). For this month-long period, the Wind spacecraft was travelling on orbits that carried it through the nightside magnetosphere at perigee, allowing it to make remote observations of the AKR source region, as well as other opportunities to observe AKR from other local times (LT). Although it is not possible to apply previously-developed GP techniques for spinning spacecraft to AKR observations with Wind, a selection technique based on the observed variability on timescales of seconds has been developed and applied. This has provided an effective selection of AKR emission, allowing a quantitative analysis and comparison to be performed. Here we focus on the unique dual-vantage-point of this Cassini-Wind conjunction during 1999. In Section 2 we describe the instrumentation, the calibration of the radio data, and the selection technique which we have applied to extract AKR. In Section 3 we compare and contrast the viewing geometry and observations of Wind and Cassini as they traverse the terrestrial magnetosphere on different paths. In Section 4 we summarise our findings and interpretation of the complementary data.

2 Instrumentation and Empirical Data Selection Technique

The Wind spacecraft, launched in 1994 as part of the International Solar Terrestrial Physics (ISTP) mission, is equipped with various instruments designed to study the solar wind and radio emissions from both the Sun and Earth. The primary function of the spacecraft is that of a solar wind monitor, and Wind has most often observed from the Lagrangian point L1 (sunward of Earth); Wind first reached L1 in 1996 before spend-

ing time between 1998 and 2004 executing complex orbital manoeuvres to explore Earth's magnetosphere. The spacecraft returned to L1 in 2004 and has been there since. The relevant instrumentation will be described first in section 2.1 before the appropriate calibration steps are described in section 2.2. The method of selecting radio data pertaining to AKR is then illustrated in section 2.3.

2.1 Wind/WAVES Radio Instrumentation

The WAVES investigation (Bougeret et al., 1995) is comprised of two antennae in the spin-plane of the spacecraft (X and Y - with original tip-to-tip lengths of 100 m and 15 m, respectively) as well as one aligned with the spin-axis (Z, of length 12 m tip-to-tip). The antennae used here are of the electric dipole type, each formed of two monopolar wire lengths along the same axis on either side of the spacecraft. Of the three WAVES radio receivers RAD1 operates between 20-1040 kHz, covering the whole AKR frequency spectrum, and utilises antennae that are each in the short-antenna regime, allowing for a beaming pattern that is independent of the observation frequency.

The RAD1 receiver can operate in one of two modes: the SEP mode allows the receiver to measure with one of the equatorial antennae (usually X) and the Z antenna independently. The SUM mode performs the electronic summation of the X and Z antennae, outputting this synthetic signal as well as one with a $\frac{\pi}{2}$ phase shift applied to the equatorial antenna. The SUM mode thus returns two signals from the synthetic inclined dipole. In this work the original SUM signal will be referred to as the S antenna and that with a phase-shift applied as the S' antenna. RAD1 has 256 available frequency channels between 20-1040 kHz and channels can be chosen to sample the radio environment via three different methods. The most often used allows the instrument to be provided with a list of frequencies to be measured over the next fixed-duration sweep cycle of samples.

Each frequency channel is measured at each antenna over the respective integration time (154 ms for the S and S' antennae and 308 ms for the Z antenna) to comprise a single observation. Measurements are then repeated at that frequency across one spacecraft rotation in order to receive a signal that corresponds to a single period of modulation. Sampling all 256 frequency channels, while offering greater spectral resolution, would increase the duration of the sweep cycle and so decrease the temporal resolution. The typical total time attributed to the measurement of a single frequency for S, S' and Z antennae, accounting for the offset incurred at the beginning of the frequency sample, is 358 ms. A sweep cycle, lasting $\sim$3 minutes, is typically comprised of 64 frequency measurements, each made during one spacecraft spin period. Thus a total of 8×64 voltage spectral density measurements received by each of the S, S' and Z antennae, as well as the corresponding times of measurement, are supplied for a single sweep cycle. Each measurement is provided in units of $\mu V^2 Hz^{-1}$ and the preamplifier and receiver gain values have been taken into account. As well as this, general data including spacecraft attitude parameters and indicators for the mode of operation of the RAD1 receiver are supplied with each sweep cycle. L2-level data for the RAD1 instrument are provided as $\leq 480 \times 3$ minute sweep cycles that comprise 24 hours of RAD1 observations.

2.2 Source Flux Density Determination and Calibration

2.2.1 Background determination and subtraction

The frequency range of the RAD1 receiver is such that background radio emission is present due to both the local plasma environment and non-thermal emission from the galactic center or disk. At lower frequencies (below $\sim$ 300 kHz) the thermal motion of charged particles in the plasma surrounding the spacecraft creates quasi-thermal noise (QTN) (Meyer-Vernet & Perche, 1989) while emission from the galaxy dominates at higher

frequencies (Novaco & Brown, 1978; Cane, 1979). Previous examination of measurements across the entire WAVES frequency range has consolidated the measured galactic spectrum with previously derived functional forms (Dulk et al., 2001) and more recent measurements across the RAD1 receiver show agreement with a spectrum that falls off between 100-200 kHz (Hillan et al., 2010). Hillan et al. (2010) produced a complete background spectrum, combining models of both the galactic background and the QTN. A two-component model was used for the QTN that defines the signal above and below the plasma frequency; at the lower frequencies the QTN intensity spectrum may vary as the Wind spacecraft travels through regions of differing plasma density within the magnetosphere, magnetosheath and solar wind. The intensity of the galactic background emission is expected to remain approximately constant as the orientation of the WAVES antennae is fixed with respect to the galactic source.

As the QTN is due to motion of constituents of the ambient plasma surrounding the spacecraft, it can be viewed as isotropic on average. The galactic spectrum, however, is dominated by either the galactic center or the galactic poles, dependent on the frequency of observation. Manning and Dulk (2001) use the modulation pattern to determine the galactic source of background emission at various frequencies, finding that emission from the galactic poles dominate the spectrum at >400 kHz. A similar method to that used by Zarka et al. (2004) to determine the galactic background present in the Radio and Plasma Wave Science (RPWS) instrument of the Cassini spacecraft is implemented here for all frequencies. A background spectrum is formed for every 24 hour period of RAD1 data by taking the 5% quantile at each frequency channel. Although no explicitly quiet period is selected over which to take the quantile (as opposed to the method of Zarka et al. (2004)), the definition of the quantile imposes that the remaining 95% of received signal is above this level. Although some examples of L2 data contain consistently high emission for the corresponding day at many frequencies, background spectra produced in this way agree well with other measured background levels observed by Wind, as well as producing the expected form due to the QTN and galactic background source described previously (Hillan et al., 2010). Once the background spectrum has been determined, the relevant value is subtracted from each of the eight measurements made during a spin period, implicitly assuming isotropy of the background source. If the data is negative, so unphysical, following background subtraction, the background value at the given frequency is stored instead.

2.2.2 Calibration

To relate the received power of the WAVES instrument to the AKR flux density, we consider the GP technique developed by Manning and Fainberg (1980). GP techniques allow for radio source parameters to be determined by inverse modelling the observations to the radio source parameters using the antenna reference frame and a model of the emission geometry. In their work, spin measurements from a synthetic inclined dipole (here fulfilled by the WAVES S antenna) and a phase-shifted inclined dipole (S') antenna are demodulated and combined with a spin-axis-aligned (Z) antenna to derive the Stokes parameters (flux density and the degrees of linear and circular polarisation), angular coordinates and the angular radius of the source, so describing the state of a partially-polarised extended source. To derive these parameters, it is assumed that a single radio source is observed by the instrument and that the source parameters are constant as the spacecraft completes a spin such that the modulation pattern can be inverted. For AKR this assumption is often broken; either the intensity of the source is variable on timescales lower than that of the spin, or the spacecraft is observing emission from multiple sources in each measurement as it changes position during a spin, or a combination of the two (see Section 2.3). It is not possible to use the combination of the WAVES antennae in this case as the exact variability over the modulation pattern cannot be determined analytically without *a priori* knowledge of the source parameters. However, the spin-axis-aligned Z antenna can be used to determine the source flux density after modifications

are made to the original GP inversion. We assume that, for an AKR observation, the radio source is a point source and there is no linear polarisation. Following from equation 21 in Manning and Fainberg (1980), this gives

$$P_Z = \frac{1}{2} G S_Z \sin^2 \theta \tag{1}$$

where P_Z is the power measured by the Z antenna, G is a calibration factor, S_Z is the flux measured by the Z antenna and θ is the co-latitude of the radio source. For AKR, we can assume that the source region is approximated by the Earth's center and transform the source co-latitude θ to λ, the latitude of the spacecraft in geocentric-solar-ecliptic (GSE) coordinates. This then gives

$$P_Z = \frac{1}{2} G S_Z \cos^2 \lambda \tag{2}$$

as the received signal of the Z antenna, oriented normal to the ecliptic plane, is minimised when the spacecraft is above the poles. This then gives the flux density S_Z for each of the eight spin measurements, which are then averaged using the mean.

The synthetically-inclined S (and phase-shifted S') antenna is longer and more sensitive than the Z antenna, making its measurements prone to spurious signals at all frequencies as receiver electronics are saturated. This is often the case when Wind observes the highly intense AKR, which for this study occurs mostly when the spacecraft is near perigee. This contamination does not occur with the shorter, less sensitive Z antenna. While the Z antenna is less prone to saturation, its lower sensitivity means that previous methods of calibration with Wind/WAVES cannot be used. These have employed measurements of the galactic background to determine a value of the instrument gain, using a model of the galactic emission to infer the observed flux during a quiet period and then equate this to measurements (Zarka et al., 2004; Zaslavsky et al., 2011). The shorter Z antenna typically measures the galactic background to be within 10 dB of the instrumental noise, as given by the received power prior to antenna deployment, so the contribution from the galactic signal cannot be determined. For this reason, the initial measurements of the instrumental characteristics are used to determine the gain using

$$G = (\frac{C_a}{C_a + C_s})^2 L_{eff}^2 Z_0 \tag{3}$$

where $Z_0 \sim 120\pi$ is the impedance of free space, C_a and C_s are the antenna and stray capacitances, respectively, and L_{eff} is the effective length of the antenna. Here we use the physical length of the antenna, given that both electrical monopoles that comprise the Z antenna are in the short-dipole regime, so that $L_{eff} = L_{phys}$.

As the above uses measurements from only a single antenna instead of the complete antenna geometry, without a complete model of the radio source emission, the flux S_Z calculated with equation 2 can only be attributed to the Z antenna measurement and not a representation of the true source intensity. A better constrained value of the source flux density can be obtained by comparing observations of solar radio Type III bursts, which can act as a reference for cross-calibration given the expected uniformity of the signal and distance of both spacecraft from the source. The calibrated fluxes here were compared with data produced by a direction-finding inversion that is bespoke to solar Type III burst observations with Wind, giving the flux density, angular coordinates and angular extent of the source. By comparing the average spectrum of peak fluxes across a set of Type III bursts, a scaling factor can be applied to the data as calibrated with the Z antenna alone and used in this study. Details of the approach taken to produce the average spectrum can be found in Appendix A.

2.3 Empirical Selection

As mentioned in section 2.1, the Wind/WAVES Z antenna is spin-axis aligned. As the spacecraft rotates, antennae in the spin-plane observe a modulating signal that is dic-

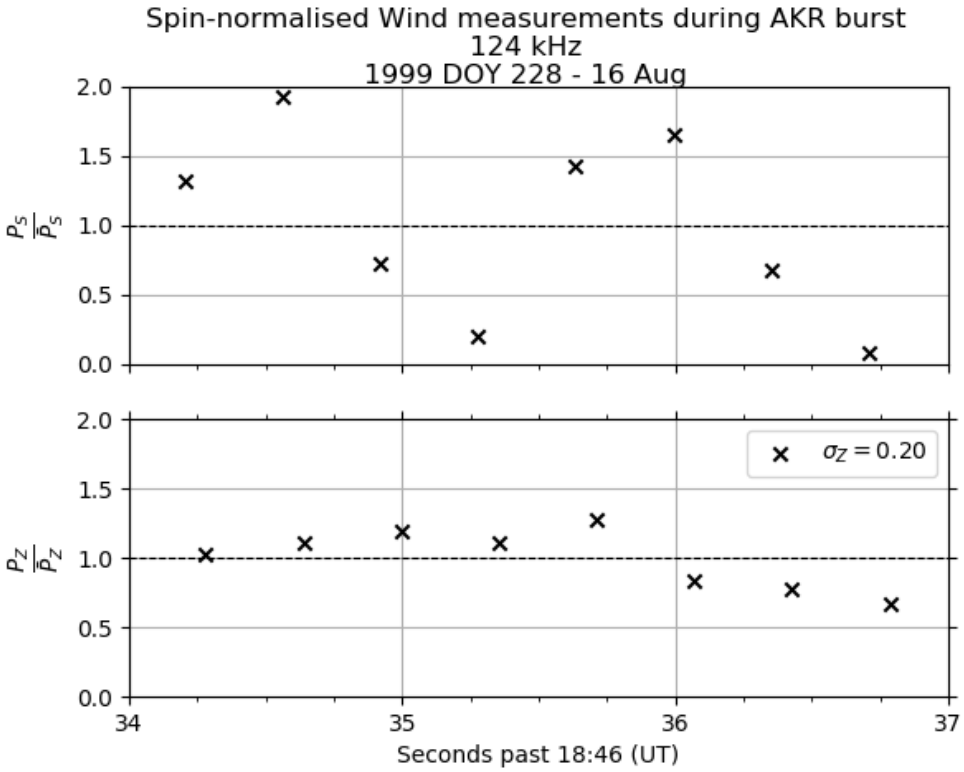

Figure 1. Measurements (P_S, P_Z) made by the synthetic-inclined (S) and spin-axis-aligned (Z) antennae of Wind/WAVES during a single spin, normalised by the average received power during this time ($\bar{P}_S$, $\bar{P}_Z$), and corresponding to a single sample at 124 kHz of the latest burst of AKR emission in figure 2a. The value of the selection metric, σ_Z, is given in the legend of the bottom panel.

tated by the rotation period and the position of the antennae with respect to the source location and other parameters. While this modulation can be used to derive source parameters using GP inversion as previously mentioned, these require that the source parameters are constant during a spacecraft rotation; a constraint which is often broken for AKR. The spin-axis aligned Z antenna sees no such modulation due to the spacecraft rotation, and so any variability in the received power can be attributed to changes in the intensity of a radio source, assuming that a single source is observed. It has been mentioned that the spacecraft measures a superposition of multiple spatially-separated sources, limiting the observations by the temporal and spectral resolution of the instrument. Although this is less true for the spin period than it is for the sweep duration, it is possible that the variability measured by the Z antenna for a spin is due to the more slowly varying intensity of separated sources. Given the generation mechanism of AKR, however, it is likely that a single source will have a highly varying amplitude on spin timescales of seconds. While it is non-trivial to discern between the two effects, it is important to note that this may also lead to an overestimation of the AKR selection, although this effect is negligible when data are averaged over the sweep duration.

A statistical proxy for AKR can be derived from the Z antenna by modelling the 8 measurements made during a single frequency sweep as a normal distribution centred on a mean intensity, with any variability then being described by its standard deviation σ. To be able to compare the standard deviation between sources of different mean in-

tensities, the measurements are normalised by the mean intensity of the spin. This gives σ_Z, the standard deviation of the spin-normalised Z antenna measurements. Figure 1 shows the spin-normalised measurements made by the S and Z antennae during an exemplary AKR burst (also seen in figure 2a). It is not clear from the figure that the S antenna is displaying an insufficient modulation pattern to derive the GP source parameters and an analytic relationship between the S and Z measurements is not known. However, the variability across the Z antenna measurements shows that the observations do not meet the criteria of constant intensity for GP inversion, and the σ_Z value for this spin is given in the legend of the bottom panel of figure 1. While a comprehensive study of the σ_Z distribution is not included, examination of the dynamic spectrograms show that the Z antenna consistently measures higher variability (using σ_Z) during periods of AKR bursts. To select regions that correspond to AKR emission, a numerical threshold is chosen based on visual identification of the dynamic spectrograms from Wind during the Cassini flyby; here $\sigma_Z \geq 0.1$. See Appendix B for further justification of the choice of the threshold value. While σ_Z acts as a proxy for the radio source here, we note that without access to the GP inversion and polarisation information we cannot make an exact physical inference and so the selection is empirical. With average $sigma_Z$ spectra for each sweep, a mask can then be created and applied to the calibrated flux densities to select data that meets this criteria; here the flux densities are also averaged across the 3 minute sweep cycle. In this case the consideration of multiple spatially-separated sources cannot be ignored, and the flux spectra represent the spatial average of AKR emission across a relatively wide longitude as well as a temporal average.

Figure 2 shows two examples, A and B, of 24 hours of calibrated Wind/WAVES data (top panel) with the variability proxy σ_Z (middle panel) and the application of the resulting mask (bottom panel). Wind observations in both A and B contain many Solar Type III bursts with various drift rates that at times cover the entire RAD1 frequency range, as well as increases in QTN and emission at the plasma frequency at frequencies < 100 kHz. The middle panel shows the effectiveness of σ_Z as an identifier of AKR emission, with observations of Type III bursts exhibiting a standard deviation less than that of the AKR by about an order of magnitude. AKR is generally more intense than Type III bursts, and this couples with the aforementioend considerations of the AKR generation mechanism and viewing geometry to produce the observed discrepancy. While not shown here, the 52 kHz channel has persistently higher σ_Z due to radio frequency interference (RFI). In figure 2 (and figure 5), the 52 kHz channel has been removed and the values of σ_Z in neighbouring channels used to interpolate an updated 'background' value to increase visual clarity. For the remaining analysis, after selecting the AKR data with the σ_Z criterion, flux densities from the 52 kHz channel are removed to avoid contamination. AKR can be seen in both examples; in A, Wind is approaching perigee at around 1600-1700 LT and 4° latitude, and emission is observed for 11 hours between $\sim$ 80−800 kHz; it exits perigee in B, crossing 0800-0900 LT around $-6°$ latitude, and observing more sporadic emission patches throughout the day across a narrower frequency range, $\sim 100 - 500$ kHz.

Given that the metric for selection, σ_Z, is determined using the variance of measurements made during a spin, there are other sources of emission that could be responsible for the retention of a particular sample. Instrumental RFI is an example of this, but particularly rapid changes in intensity due to energetic fluctuations in the local plasma can also produce signatures similar to those produced by AKR. Particularly when Wind travels through the turbulent, dense plasma in the magnetosheath (see $\sim$DOY 229-231 and 251-254 in figure 5) the majority of the emission at lower frequencies is retained. At times when Wind is on the dayside, within the solar wind, emission is occasionally selected that has no observed, corresponding AKR signal at higher frequencies, and is assumed to be caused by similar local and temporal variations in the plasma. Intensification of the signal at other characteristic frequencies of the plasma are also occasionally seen and retained by the selection, such as emission at the plasma frequency. The re-

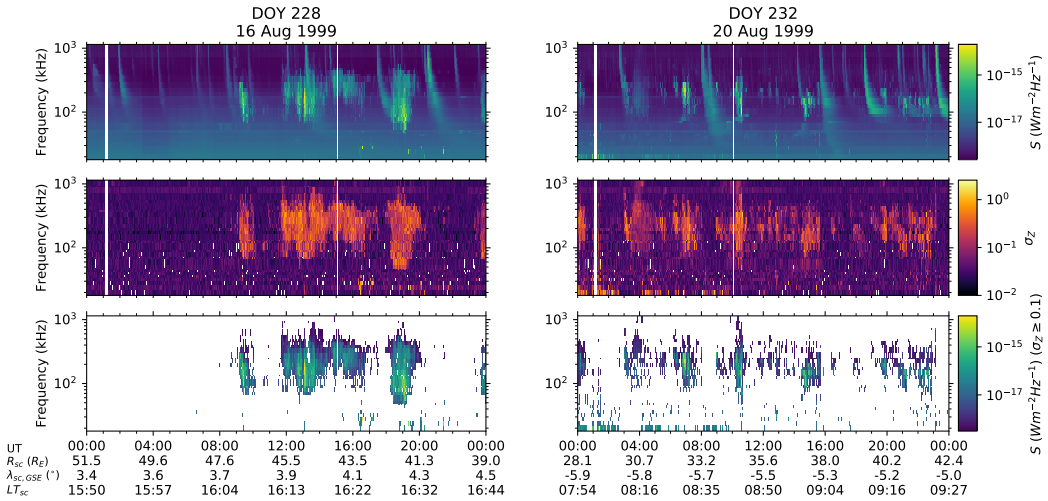

Figure 2. Two examples of application of the empirical selection detailed in section 2.3 to 24 hours of Wind data (3 minute resolution). For each example A (left) and B (right) the top panel shows flux density observed by Wind and derived by the method outlined in section 2.2, the middle panel shows σ_Z, the statistical proxy of the source amplitude variability, and the bottom panel shows the flux density with the selection mask applied (see section 2.3). The lower limit of the colour-bar of the middle panel is set at 10^{-2} for visual clarity. The radial distance, ecliptic latitude and local time for each example are shown in the ephemeris at the bottom of the plot.

tention of non-AKR signals is lessened at higher frequencies, where Wind typically sees contributions from AKR, other planetary radio emission which is often faint, or solar radio bursts which have a relatively shorter variability on the spacecraft spin period. Given that the solar radio type III bursts are removed effectively this technique is powerful, given their ubiquity and the simplicity of the selection criteria used here, and applying the flux-density calibration and selection of AKR to Wind/WAVES observations since 1994 forms a unique dataset to investigate AKR characteristics. The next section takes advantage of the selection to make an initial comparison to AKR radio measurements obtained by Cassini in 1999.

3 Application to Wind/WAVES for Multipoint AKR Observations with Cassini

3.1 Spacecraft Ephemerises

Figure 3 shows the trajectories of both Cassini (3a) and Wind (3a) projected onto the ecliptic plane for most of the period studied by Lamy et al. (2010). In figure 3b, the solid line shows the magnetopause location, using the model of Shue et al. (1998) and solar wind data from OMNIWeb with average parameters used for the period. The dotted line shows the bowshock location, derived using similar data and the model of D. J. Wu et al. (2000). The legend in figure 3b marks the location of Wind at the start of particular days of note, namely the first (DOY 227 in blue) and last (DOY 257 in red) days of the period. Also indicated are the days of Cassini's closest approach to Earth (DOY 230 in orange) and the last day of the Cassini trajectory shown in figure 3a (DOY 241). After traversing the dawn flank of the magnetosphere and passing Earth, Cassini continued downtail between 0100 and 0200 local time (LT) at $\sim 9\ R_E/h$. Figure 4 shows

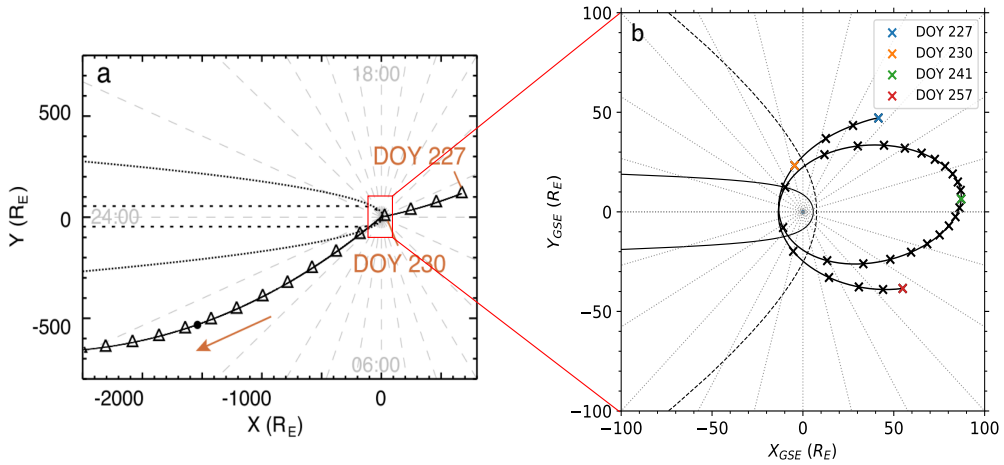

Figure 3. Trajectories, projected onto the ecliptic plane, of Cassini during the first 15 days of its flyby (a) and of Wind for the 30 day period studied (b). Triangles (a) and crosses (b) represent the beginning of each day of year (DOY). The beginning of the period, DOY 227, and the date of closest approach, DOY 230, are labelled in (a), while corresponding days are marked in colour in (b). Also coloured in (b) is the last date visible in (a), DOY 241, and the last day of the period, DOY 257. Average modelled magnetopause and bowshock surfaces are shown as dotted and dashed lines respectively.

the latitudes of both spacecraft in both geocentric solar ecliptic (GSE) and geocentric solar magnetic (GSM) coordinates.

During Cassini's flyby of Earth and the 30 day period studied by Lamy et al. (2010), from 15th August to 14th September 1999 (DOY 227 to 257), Wind completed close to two petal orbits with a perigee radii of $\sim 13\ R_E$ and apogee radii of $\sim 88\ R_E$. At the start of this period, Wind approached its first perigee from a position duskward of Earth at roughly 1500 LT on DOY 227, with a geocentric-solar-ecliptic (GSE) latitude of 3.0° and a radial distance of 67 R_E. From there, Wind approached the magnetosphere and crossed the bowshock and magnetopause before the first perigee was reached. Wind reached perigee around 0100 LT, at a GSE latitude of 1°, while traversing the magnetotail. Wind then exited the magnetosphere, covering the dawn flank and reaching apogee on DOY 241 at a GSE latitude of −0.4° around 1200 LT. After 23 days Wind reached 1500 LT once more at a closer radial distance of 44 R_E and a GSE latitude of 4.6°. Entering the nightside magnetosphere for the second time during the period, Wind reached a second perigee on DOY 252 at 0000 LT and close to the ecliptic plane. Wind then exited the magnetosphere once more, and the final observations that are conjunct with Cassini are made at around 1000 LT with GSE latitude of −3.0° and a radial distance of 67 R_E.

As mentioned in section 1, GP inversions have been successfully applied to observations from Cassini and allowed the circular polarisation of the radio emission to be determined and thus the hemisphere of origin. For the empirical selection of AKR emission, used here with Wind, there is no unambiguous way to determine the circular polarisation from the flux measurements. Due to the anisotropic, widely-beamed emission from the AKR source regions along magnetic field lines, visibility of the emission from

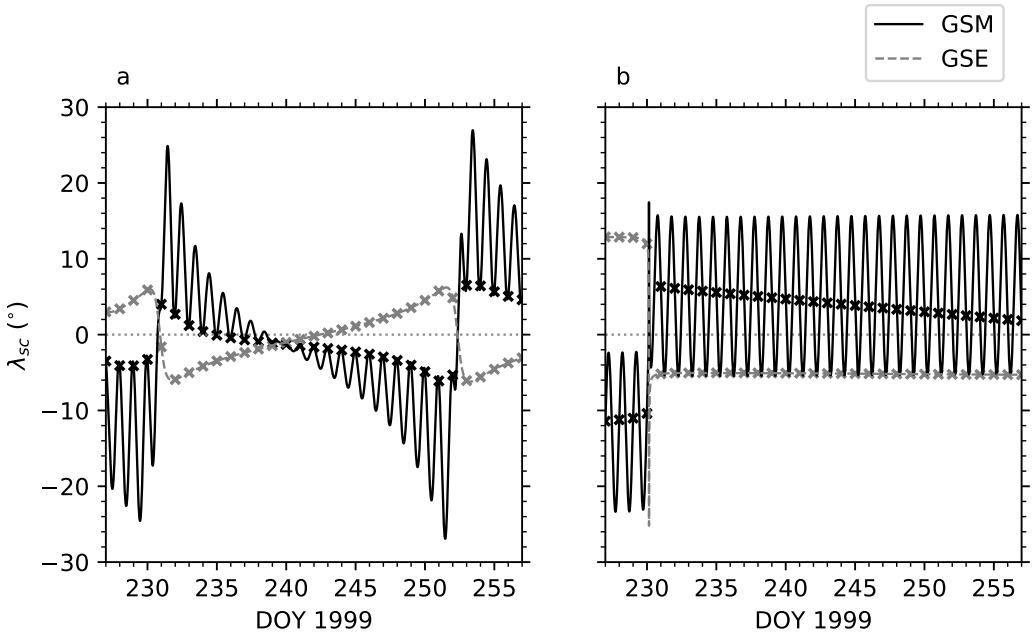

Figure 4. Latitudes of the Wind (a) and Cassini (b) spacecraft for the period shown in geocentric (GSE) coordinates with the grey, dashed line and magnetic (GSM) coordinates with the black, solid line. Markers show the beginning of each day.

either pole is highly dependent on the magnetic latitude of Wind, and inferences of the origin of the emission can be made based on this. While Wind is on the dayside, approximately between the two perigees at DOY 231 and DOY 252, it covers an increasingly narrowing range of low magnetic latitudes in first the Northern then the Southern magnetic hemispheres, crossing the magnetic equator near the apogee (see figure 4). In both cases where Wind crosses the nightside, where AKR is expected to be most visible, the spacecraft approaches from the dusk flank in the Southern magnetic hemisphere and crosses into the Northern magnetic hemisphere at perigee. Given that the magnetic latitude does not exceed 30°, it is uncertain whether or not the spacecraft will be in either or both of the regions illuminated by emission from either hemisphere. Previous examination of the average AKR source region has suggested that emission from both hemispheres can be observed at distances $> 12R_E$ in the equatorial plane (Gallagher & Gurnett, 1979), with the approximate perigee distance of Wind ($\sim 13R_E$) implying that this will be the case for all nightside observations for this period. In their study, Lamy et al. (2010) use the polarisation information to assess the average AKR power from each hemisphere when Cassini is above a given magnetic latitude. While the intensities of AKR from each hemisphere are equal when the spacecraft is near the magnetic equator, the LH emission from the Southern hemisphere was close to 4 orders of magnitude weaker than the RH (Northern) emission when the spacecraft had a magnetic latitude $|\lambda_{mag}| > 10^{circ}$. This value suggests that Wind may spend some time in the illumination region of the Southern hemisphere before reaching perigee and then in the illumination region of the Northern hemisphere as it exits the point of both perigees. For the majority of the 30 day period, however, Wind is likely illuminated by AKR emission from both hemispheres.

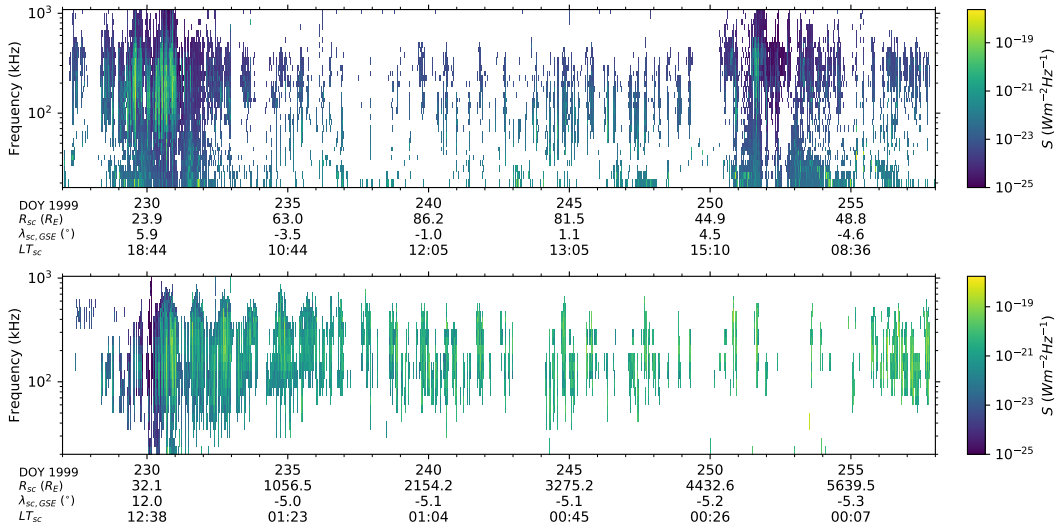

Figure 5. Dynamic spectrogram showing the flux density measured by Wind/WAVES (top) and Cassini (bottom) for 1999 DOY 227-257 and normalised to a distance of 1 AU. The top panel shows the average flux density at 3 minute resolution as selected with the σ_Z threshold described in section 2.3. The flux density is computed by calibrating the power received by the spin-axis aligned Z antenna, as outlined in section 2.2.2. The bottom panel shows the flux density observed by the Cassini spacecraft, namely the maximum of the LH or RH AKR emission of a given frequency at 90 s resolution (for complete details of the calibration and selection of AKR with Cassini, see Lamy et al. (2010)). The radial distance, ecliptic latitude and local time of each spacecraft are shown in the ephemeris at the bottom of each panel.

3.2 AKR Flux Density and Power

Figure 5 shows the AKR flux density of both Wind and Cassini for the entire 30 day period studied here. The AKR flux density with Wind is obtained using the calibration and selection outlined in section 2. The AKR flux density with Cassini contains that of both LH- and RH-circularly polarised AKR, obtained using a GP inversion technique and selecting data with $|V| \geq 0.2$, where V is the normalised Stokes parameter describing circular polarisation (Lamy et al., 2010). The maximum of either the LH or RH AKR is shown at 90 s resolution in the Cassini spectrogram. Both flux densities are scaled for the distance from the approximate source (Earth's center) and normalised to 1 AU to enable a comparison between the two datasets. The general effect of viewing position on the AKR observations from each spacecraft can be seen here; emission is stronger and more consistent for Cassini as it travels away from Earth downtail, remaining on the nightside, while a periodic variability is seen in the Wind spectrogram as it passes the nightside during its perigees. While the day-to-day variability in the observed emission is not studied here, it is interesting to note differences between the two perigee observations. Wind sees more persistent, stronger emission for the first perigee (∼DOY 229) than the second (∼DOY 251). While this variability between orbits is not surprising given the changing solar wind conditions that affect AKR, it demonstrates the differences between observations made at different times which will clearly bias any average result with a limited selection of data.

Figure 6 shows AKR flux density spectra from both spacecraft given by statistical thresholds, namely the median spectra and those for the 90% and 99% quantiles, or increasing intensity thresholds. The top panel shows Cassini flux densities for both LH and RH circularly polarised AKR, reproducing figure 6a of Lamy et al. (2010). The middle panel show Wind flux densities returned by the selection (described in Section 2.3) applied to data from 1999 DOY 227-257. Given the anisotropy of the AKR beaming and the longitudinal distribution of AKR source regions, it cannot be assumed that each spacecraft will observe the same emission region at a given time from different viewing positions in space. To elicit a valid comparison of the reduced spectra between the spacecraft, we select Wind data such that only observations made from a similar viewing position are included; Cassini was in the region in $-23° \leq \lambda_{GSM} \leq 16°$, for a geocentric solar magnetic (GSM) latitude λ_{GSM} and within 0000 to 0200 hours LT during its flyby. A complete discussion of the flux densities observed by Cassini can be found in Lamy et al. (2010), but here we compare the main features with those of Wind.

While the Cassini spectra for both LH and RH AKR flux see a mostly shallow increase up to the peak at ~ 200 kHz, this is not the case for Wind. A consistent plateau is seen in each of the spectra in the middle panel below 50 kHz, after which the flux density increases more sharply for each quantile. The discrepancies between the spectra of figure 6 at lower frequencies can be explained by the aforementioned emission due to QTN and other excitations in the plasma that is retained by the σ_Z selection. While AKR is observed across most frequencies in the RAD1 frequency range, emission at < 100 kHz is mostly affected by contamination due to these sources. Figure 6 also shows better agreement between the two spacecraft above this frequency, the resulting range including the typical spectral peak of AKR. As well as this, the AKR emission at higher frequencies is known to be more temporally consistent and can be said to be better representative of the average AKR signal compared between remotely observing spacecraft. For these reasons, in the following, only the selected signal above 100 kHz is considered. At frequencies higher than this, discrepancies between the spectra may exist simply due to the two spacecraft primarily observing different AKR source regions as we do not expect the AKR spectrum to be constant at all LT.

Again comparing the Wind spectra in the middle panel with Cassini in the top panel of figure 6, the peak of the median spectrum agrees, existing at a frequency close to 200 kHz and close to the peak flux of the RH AKR median spectrum measured by Cassini;

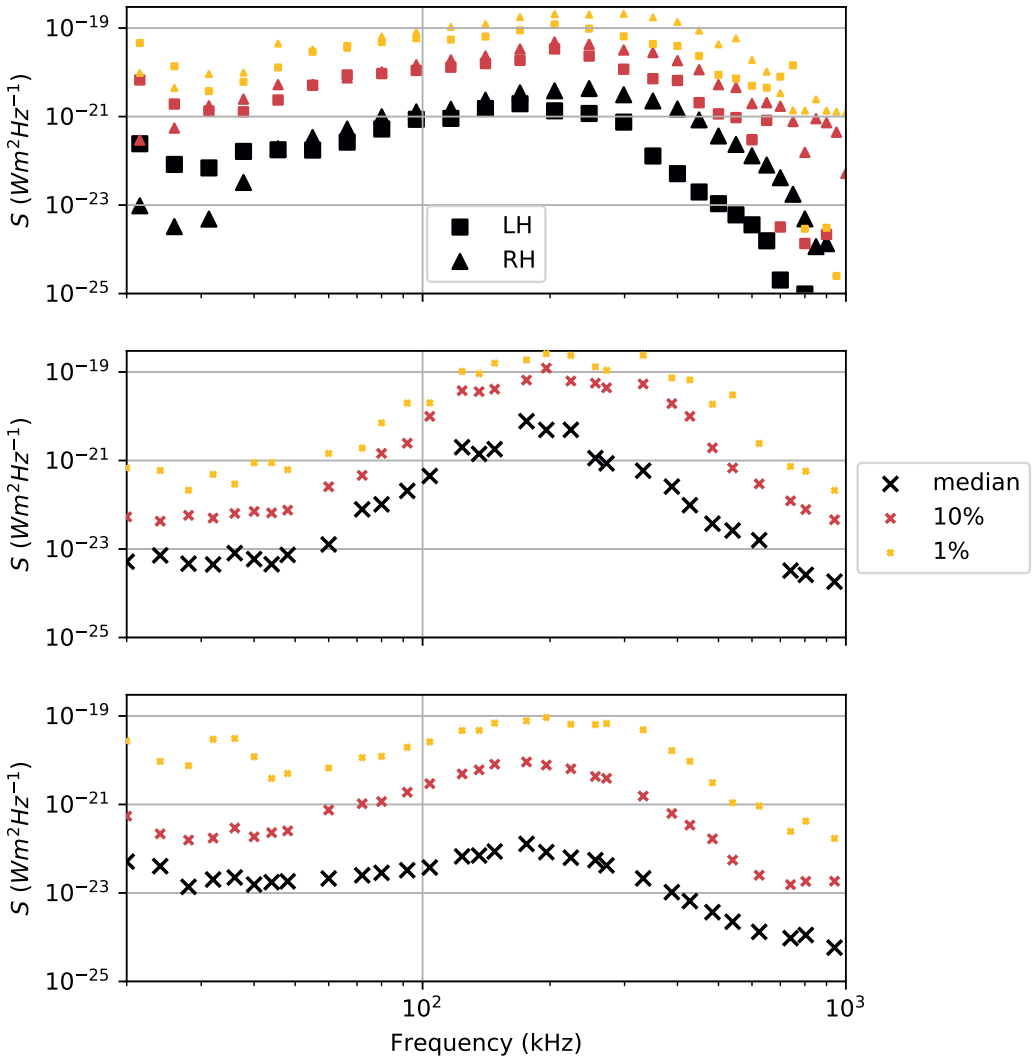

Figure 6. Reduced flux density spectra comparing AKR observations from Cassini during the whole period (top panel) with those made by Wind when in a comparable viewing position (middle and bottom panels). For this, the Wind data was further selected such that the spacecraft was located from $-23^\circ \leq \lambda_{GSM} \leq 16^\circ$ and within 0000 to 0200 hours LT. Flux density data in each case are reduced to give the measured intensity reached 50% (median - black), 10% (red) and 1% (orange) of the time. The top panel shows spectra for both the LH and RH circularly polarised AKR as given by the GP inversion applied to Cassini. The middle panel shows AKR- and position-selected data from Wind during the 30-day period studied here. The bottom panel shows AKR- and position-selected data from Wind for all of 1999, to increase the statistical rigour of the selection verification (see main text).

also in agreement with initial AKR observations (Kaiser & Alexander, 1977). While the differences at lower frequencies are likely due to contamination, the Wind median spectrum falls off more rapidly than the RH median spectrum of Cassini and is more comparable to the LH median spectrum. At the frequencies $> 700 - 800$ kHz, the Wind median spectrum is more closely comparable to the RH AKR median spectrum, although the aforementioned limitations prevent close physical interpretation of the differences or similarities between the spectra. Generally, however, the Wind median spectrum has a minimum at the highest observed frequencies, which again agrees with the Cassini measurements. Each of the Wind spectra that show the higher intensity thresholds in the middle panel show generally good agreement in magnitude with those of Cassini; a similar increase of 2 orders of magnitude between the median and highest intensity spectra is seen in the selected Wind data. This is interesting considering the small amount of time Wind spent in the region relative to Cassini, and suggests that the limited Wind measurements here are characteristic of the AKR that Cassini observes for the whole period. There is also evidence of broadening of the spectral peaks to higher freqencies with increasing intensity in the middle panel and, while it is less clear, a shift of the peak to higher frequencies as observed by Cassini.

Given that Wind spends the least amount of time on the nightside during perigee for this period, it is important to consider the limiting effect of the position selection. To highlight this, while Wind spends $\sim 1.2\%$ of the time in the specified region during this 30 day period, 5.1% of the AKR data selected here is observed in this region. However, this increase shows the efficacy of the empirical selection in reflecting the preferential location of the nightside for observing AKR emission and the AKR sources themselves. Although we cannot compare the Cassini spectra with Wind observations made outside of the temporal range covered by the Cassini flyby, increasing the scope of the data included can allow us to characterise the selected data more rigourously by comparing the general features of the spectra. For this reason, the bottom panel of figure 6 shows spectra defined by the same thresholds but applied to Wind data from the entirety of 1999 after selecting the AKR as described. Although the magnitude of the spectra is lower (which is expected as more AKR emission is included, assuming that the more extreme events will happen less regularly) the broadening of the spectral peak to higher frequencies with increasing intensity is present. There is a larger increase of 3 orders of magnitude between the median and highest quantile spectra in the bottom panel, suggesting that the observations made in the 30 day period here are more intense than other times in the same year. There is also a seperate, much shorter peak around 30-40 kHz that exists in the highest intensity spectra of the bottom panel, which could be indicative of the average state of the magnetosphere or solar wind throughout 1999 as consistent Langmuir wave excitations may be seen close to the local plasma frequency in this region.

The AKR source region, as discussed in section 1, is typically found at altitudes of roughly 2000-10000 km along a given field line, corresponding to emission at frequencies 100-800 kHz. This higher frequency emission is much less transient than that of higher altitude sources that emit between $\sim 30 - 100$ kHz and are well correlated with substorm onset (Morioka et al., 2007). To characterise the AKR observed by Wind and facilitate the comparison between the two spacecraft, the selected flux data are integrated over the frequency range 100-650 kHz. While the frequency range used by Lamy et al. (2010) (30-650 kHz) encompasses both the lower frequency and main band of AKR, we increase the lower frequency limit here to mitigate the inclusion of spurious data as mentioned above. While this does not allow for a direct comparison between the integrated powers of Wind and Cassini, it enables general characteristics of the AKR, such as the viewing geometry and temporal modulations, to be studied. With a more refined selection of AKR signal at frequencies below 100 kHz, the power can be integrated over a frequency range such as 30-100 kHz to investigate the lower frequency AKR component. Given that the integration time of each flux density measurement is the spin period of

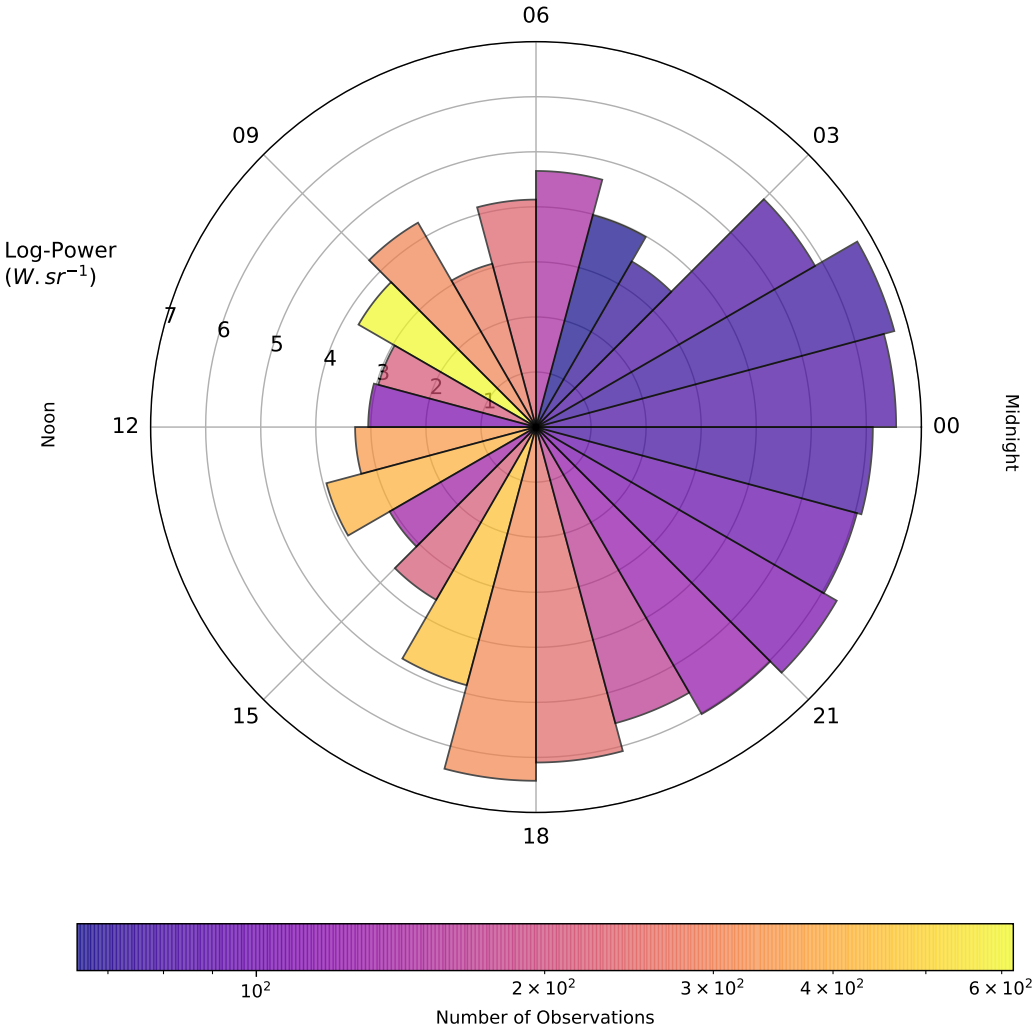

Figure 7. Log power in Wsr^{-1} integrated across the range 100-650 kHz for the AKR flux (as selected by 2.3) and averaged in LT bins 1 hour wide. The sun and noon sector is to the left, while the midnight sector is to the right in these plots. Colours show the number of 3-minute-resolution observations, retained by the empirical selection, in each LT bin.

the spacecraft, the power can be integrated by simply taking the mean of the flux densities and integrating over the frequency channels. As the AKR beaming is anisotropic and knowledge of the exact source region for each measurement with Wind is unattainable, we cannot integrate the power over solid angle and so present the power in units of Wsr^{-1}.

3.3 AKR Viewing Geometry

Figure 7 shows the integrated power data described in the previous section 3.2 after taking the mean power in 1 hour spacecraft LT (GSE) bins and plotting the $\log_{10}$ power as a rose plot; the noon and midnight sectors are on the left and right of the figure, respectively, and the dawn and dusk sectors are on the top and bottom. A large asymmetry can be seen in the selected power with a 3 order of magnitude increase of the LT bins between 1700 to 0300 over those on the dayside that have the lowest powers. The

broad picture of figure 7 is thus consistent with previous findings which suggest that the source regions are located on the nightside and beam anisotropically (Alexander & Kaiser, 1976; Gallagher & Gurnett, 1979; Mutel et al., 2004, 2008). Also of interest here are the bins at 2100 and 2200 hours LT, in the centre of the range of intense emission. This corresponds to previous observations of the LT of the source regions most favoured by AKR sources (Panchenko, 2003; Mutel et al., 2004), as well as the average LT of the most intense AKR source region at 2200 MLT (Green, 2004). Given the illumination region of an AKR source, and that the observations here are made from comparatively large radial distances and with a swept frequency receiver, it is expected that the emission from an AKR source could be measured by Wind from a neighbouring LT sector. At Saturn, this longitudinal difference has been observed to be up to 2 hours LT (Lamy, Zarka, Cecconi, Prangé, et al., 2008; Kimura et al., 2013). The location of the centroid of the most intense average power in figure 7 is an indication of the effectiveness of the AKR selection used here.

While AKR has been previously observed from the dayside it can be difficult, without polarisation information, to discern whether this emission is attributable to the illumination of the spacecraft by a source on the nightside via either emission viewing geometry or scattering, or that of a dayside source (Hanasz et al., 2003; Mutel et al., 2004; Schreiber et al., 2017). Deducing the exact origin of the source of emission is complex and is not possible within the scope of this study. However, the dynamic spectrogram in figure 5 as well as the distribution of average power in figure 7 show that we can observe AKR at all LT, with some of the most intense observations on the dayside made when Wind was near both the noon-midnight meridian and ecliptic plane.

The colour of each LT bin reflects the number of data used to compute the average, where each data point represents the power of each 3 minute frequency sweep. The orbital dynamics of the spacecraft produce the overall colour distribution, with perigee on the nightside limiting the number of observations that can be made and vice versa on the dayside. For this reason more total observations will be made on the dayside, but fewer of those observations will be selected given the preferred nightside location of the AKR source regions. This is seen when taking the ratio of the number of observations made in a local time sector with the number of selected data from the same sector. For the observations made on the dayside ($0600 \leq LT < 1800$) an average of 38% of data is retained by the selection, while 83% of nightside observations ($1800 \leq LT < 0600$) are retained by the selection. The variation in the number of selected data in the noon sector in figure 7 shows that the distribution here may not be indicative of the true average AKR power, as temporal variability of the state of the magnetosphere system will bias this count as the spacecraft crosses the dayside once during the 30 day period studied here. As discussed in Section 3.1, Wind crosses the nightside twice during this period, so the data contributing to the average on the nightside are comprised of two seperate samples of this region. Further discussion of the power distributions that produced the averages for each LT bin can be found in Appendix C.

3.4 AKR Temporal Modulation

Figure 8 shows the result of a fast fourier transform (FFT) when applied to the Wind integrated power over 100-650 kHz and considering the entire 30 day period. A moving average is taken over a centred 3 hour window in order to smooth the data, removing local temporal variability. Given that the integrated power can vary over several orders of magnitude the FFT is performed after log-transforming the data, as done in Lamy et al. (2010) to reduce the weight of this variability on the analysis. The relative spectral power is shown, having normalised the FFT output by the maximum spectral power found at a period of 24 days (576 hours), denoted by the vertical grey dotted line, and corresponding to the approximate orbital period of Wind during this time. The presence of a peak at this period can be explained with reference to figures 3b and 5; the perigee

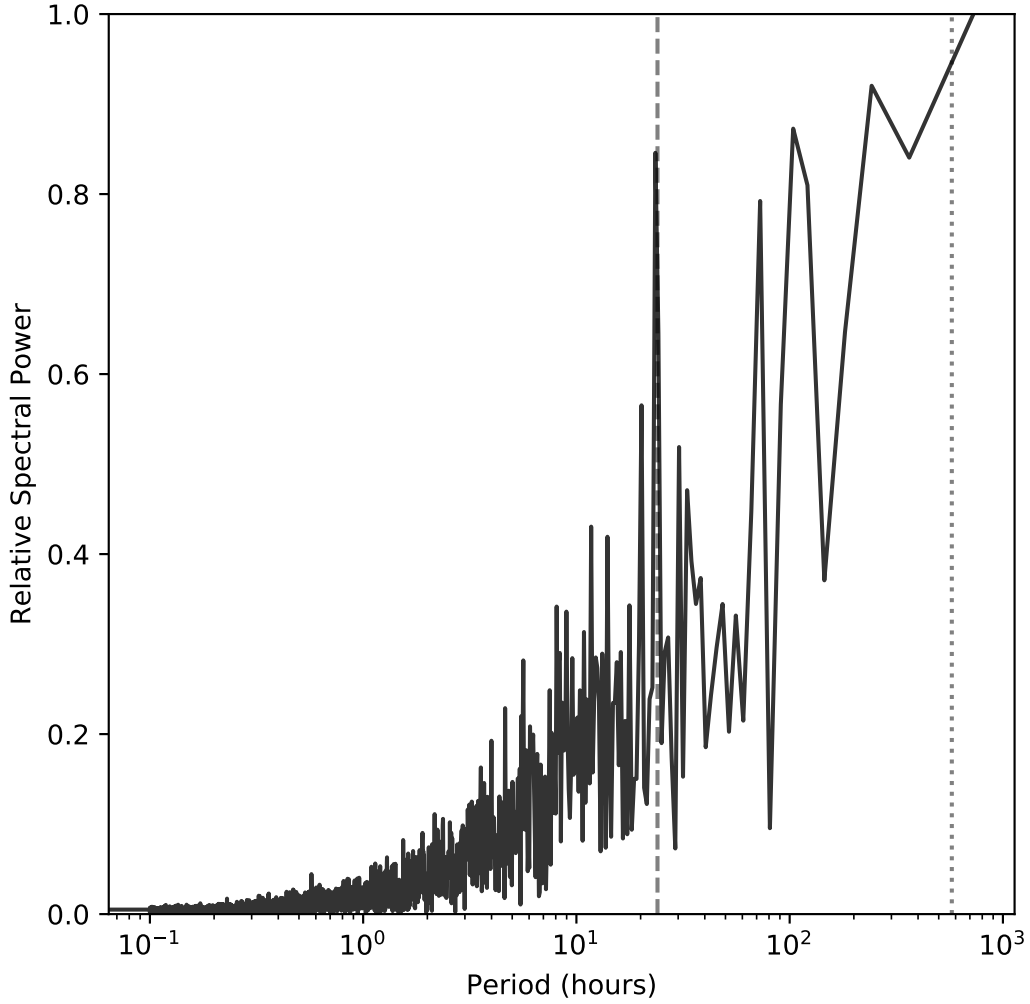

Figure 8. Fast Fourier Transform (FFT) of the integrated power over 100-650 kHz for the whole period. Analysis is performed on the integrated powers after applying a 3 hour rolling window and log-transforming the data. The relative spectral power is shown; powers are normalised by the value at the peak, here at $\sim$ 24 days (= 576 hours). The integrated power is input at 3 minute resolution; data where no AKR is present are set to $P = 10^{-8}$ Wsr^{-1} to include them in the analysis. Vertical grey dashed line shows a period of 24 hours respectively. The vertical grey dotted line is at a period of 24 days, the approximate orbital period of Wind.

of Wind precesses dawnward across the nightside magnetosphere, measuring intensifications in the AKR as it passes the nightside across two to three days, separated by the dayside apogee.

The vertical dashed grey line in figure 8 highlights the peak at a period of 24 hours. Although the FFT output is noisy, particularly at lower frequencies but also at periods between 1-24 days, a peak is observed in the Wind data at 24 hours. The statistical significance of this peak was tested via bootstrapping, where the time series is shuffled randomly before undergoing the same analysis and comparing the spectral peak, allowing the null hypothesis to be tested. We found that the peak at 24 hours has a p-value of 10^{-5} and so is significant.

In the analysis of the GP inversion results from Cassini, measurements of the modulation were made at various timescales of the AKR emission from both hemispheres, including a diurnal periodicity as seen here (Lamy et al., 2010). Other observations have also noted this feature, and it has spurred debate as to whether the variability is inherent to the AKR source or that of a geometrical viewing effect as the emission cone precesses (Panchenko et al., 2009; Morioka et al., 2013). While out of the scope of this study, comparing the relative timing of the daily AKR bursts between Cassini and Wind would allow the potential origins to be examined further. Periodicities at timescales shorter than 24 hours are also observed with Cassini; short term modulations are observed that are attributed to the triggering of AKR at substorm onsets, thought to occur every few hours, and semidiurnal variability was also observed. Lamy et al. (2010) found, using circular polarisation information, that RH and LH AKR exhibited a diurnal periodicity in antiphase as well as a semi-diurnal periodicity in the LH emission. With Wind, which is likely in the illumination region of both hemispheres for the period, we cannot discern the exact hemisphere of origin and so expect to see a contribution from both of these modulation effects. While peaks are seen around 12 hours in figure 8, albeit amongst noise, a similar analysis applied to a much longer dataset could be used to make further inferences about the origin of this and other periodicities. However, the presence of statistically significant, diurnal periodicity in figure 8 lends further weight to the effectiveness of the empirical selection used here, and shows its future promise for use with Wind.

4 Conclusion

We have described a new method of selecting AKR emission from the complex radio environment observed by Wind, using a statistical measure of the variability across the spin-axis-aligned Z antenna during a spacecraft spin. Examination of individual spins and the flux density dynamic spectrograms during a 30 day trajectory of Wind shows that the selection is effective at removing ubiquitous solar Type III bursts from the data and isolating AKR (figures 1 and 2). Although there are limitations at lower frequencies as RFI and sources of high temporal variability from the local plasma can contaminate the selection, the selection criterion employed here is based on a simple numeric threshold, and can be readily applied to the extensive dataset of Wind. Here we applied the AKR selection to Wind data for an interval overlapping with the Earth flyby of the Cassini spacecraft. The Cassini data have previously been treated with a full GP inverison (Lamy et al., 2010), but here they provide context for the sensitivity of radio observations to the viewing position of the spacecraft. After considering the discrepancies between the viewing positions of the two spacecraft during the period (figures 3 and 4), the flux density dynamic spectrograms of the 30 day period between Wind and Cassini are compared in figure 5. This shows the expected reduction in observed emission as Wind traverses the dayside and is no longer illuminated by the most intense AKR sources located on the nightside. Examining the data more closely, we compare the flux density spectra of Wind observations made from a comparable region to that of Cassini for the period and find that the general characteristics of the AKR spectrum are reproduced well at frequencies > 100 kHz. Figure 6 shows the broadening of the spectral peak at around

200 kHz in the median spectrum to higher frequencies for the most intense emission, agreeing with the accepted AKR spectrum and the previous Cassini observations.

Accounting for the aforementioned limitations, we integrate the flux densities measured by Wind between 100-650 kHz for each 3 minute sweep to represent the confident selection of AKR, covering the main frequency range and allowing a comparison with previous results from Cassini. We have accounted for the viewing geometry of AKR in the observations by averaging the integrated power measured in each one hour LT bin, shown in figure 7. This reproduces quantitatively the day-night asymmetry that can be seen in figure 5 and is again expected, with a 3 order of magnitude increase from $\sim 10^3 - 10^6$ Wsr^{-1}. This also provides confidence in the selection of AKR by this method given that it also reproduces the dawn-dusk asymmetry associated with the close correlation between the AKR source region and the auroral region in the ionosphere. Emission is selected at all local times, showing that we can observe AKR from many of Wind's various viewing positions in the magnetosphere and solar wind and shows promise for future studies where the selection can be applied to a larger Wind dataset and aid statistical analyses of events. Using the selected integrated power we examined the temporal variability of the Wind AKR observations. An FFT analysis produces a statistically significant ($p < 10^{-5}$) peak at 24 hours, which has been previously observed in AKR measurements although we do not comment on the origin in this study. Future work will include examining the average power with magnetic latitude in an attempt to statistically constrain the hemispheric origin of the Wind observations. Given the ease of masking the Wind data with this technique, longer-term studies of diurnal and semi-diurnal modulations can be conducted with Wind alone, which has > 2 decades of observations from a variety of positions. With the verification of the empirical selection as seen here, statistical analyses can also be conducted between resulting AKR dataset and lists of substorm onsets that cover decades and are complimentary to Wind's lifetime.

Appendix A Cross-Calibration Using Type III Bursts

As mentioned in section 2.2.2, the flux S_Z returned from the linear Z antenna must be scaled to those retrieved by a full GP inversion, in which the emission of a given source is modelled as received by the antennae system. This can be done by comparing the flux densities from the Z antenna here with those obtained by a GP inversion, using Wind also. We have access to data from such a GP inversion that assumes the source parameters of a solar radio Type III burst and utilises the entire Wind/WAVES system. To properly compare the fluxes from Z antenna, we must omit the $\cos^2 \lambda$ term from equation 2 to reflect the fact that the source direction is no longer assumed to be at Earth, and the Type III burst source region is sufficiently far enough away and close to the ecliptic plane that the Z antenna is always perpendicular to the emission. Explicitly, the Z antenna is pre-calibrated using

$$P_Z = \frac{1}{2} G S_Z \tag{A1}$$

for the observations presented in this section. The fluxes from the Type III inversion with Wind are derived using calibration from Zarka et al. (2004), which has since been corrected by a factor 2 by Zaslavsky et al. (2011) and is accounted for here. The fluxes from the Type III inversion with Cassini are similarly derived but have already accounted for this factor.

Figure A1 shows the comparison of calibrated flux densities for an example of a Type III burst observed by Wind and Cassini during 1999 DOY 240. The Wind observations are given at different resolutions; the data used here are averaged over the 3 minute sweep, while the original resolution of each frequency channel is retained in the data from the Type III GP inversion with Wind. The peak of the primary Type III burst at 272 kHz is seen close to 18:10 UT in this example, and while good agreement is seen between the Type III GP inversions with Cassini and Wind, the Z antenna-calibrated data have an

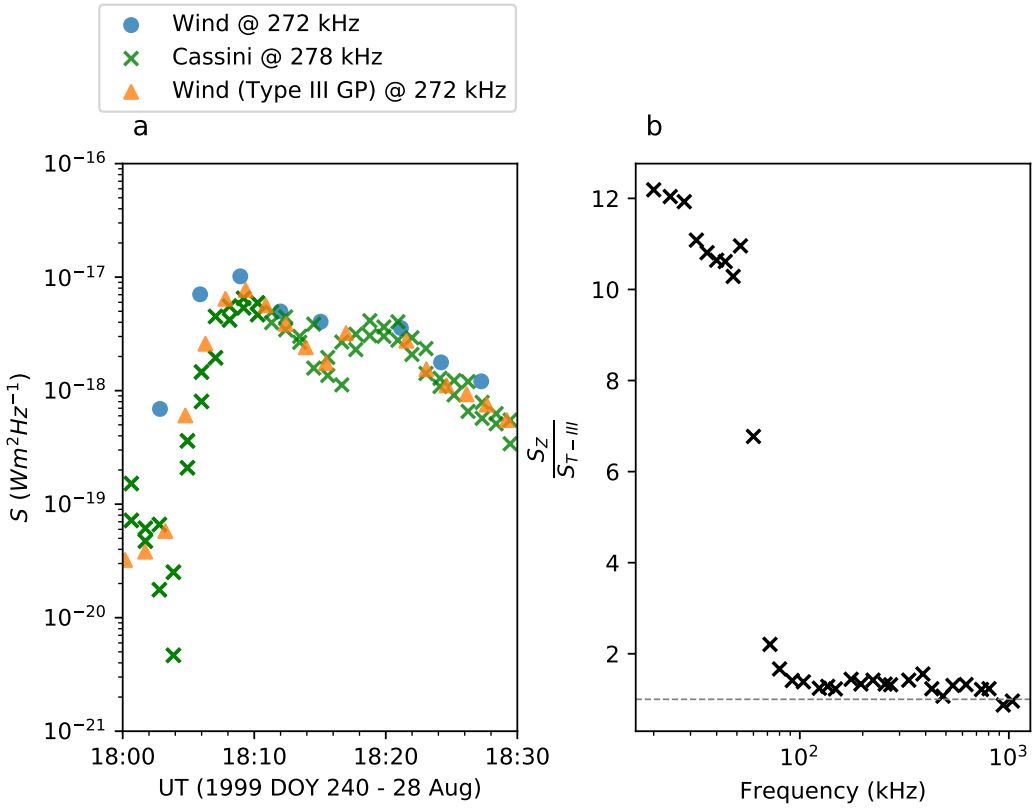

Figure A1. Comparing flux densities of a single Type III burst at comparable frequency channels between spacecraft (left) and the resulting ratio between the two datasets from Wind, using the peak flux spectra from the Type III burst (right). Included in the left panel are data derived from Wind using the calibration method described in section 2.2.2 (S_Z, blue circles), modified to account for the change in radio source (see Appendix A), data from Cassini using a GP inversion that treats Type III bursts (green crosses) and data from Wind using a similarly modified GP inversion at the original 90 s resolution of the frequency channel (S_{T-III}), orange triangles). The panel on the right shows the ratio $\frac{S_Z}{S_{T-III}}$, where each data point is given by the ratio of the peak flux between datasets during DOY 240 18:00-18:30. The grey, horizontal, dashed line is at unity.

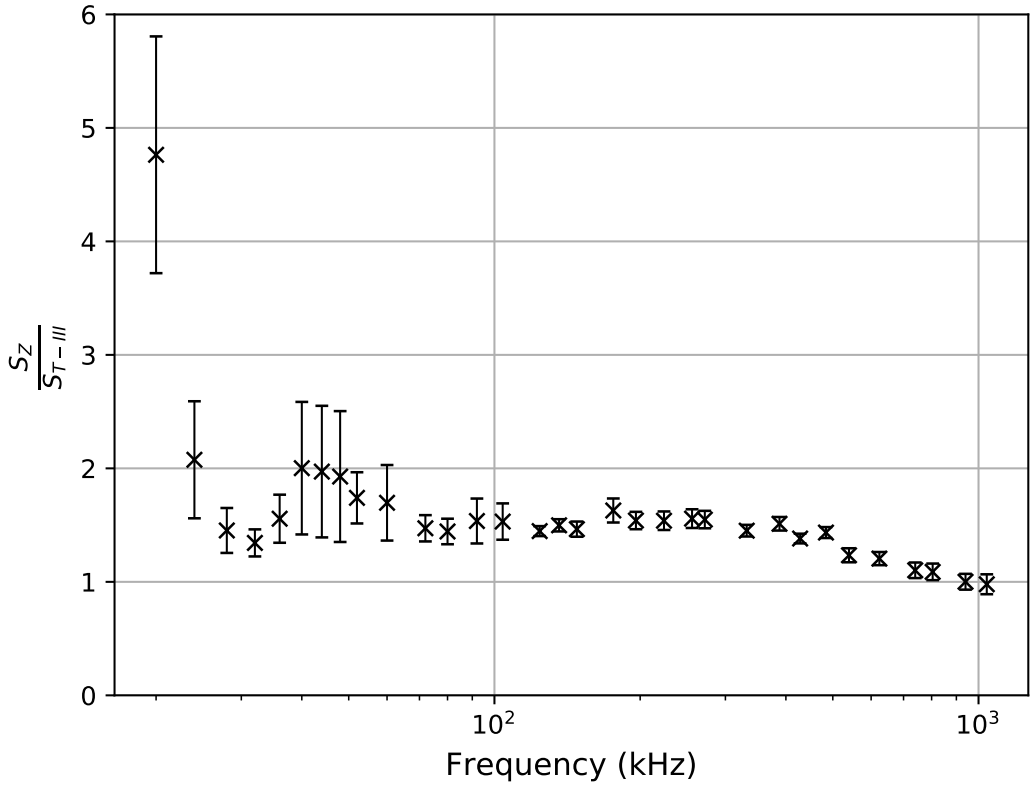

Figure A2. Spectrum of the average ratio between peak flux spectra for a total of 19 Type III bursts. As detailed in section Appendix A, each Type III example is described by a start and end time as well as its frequency limits. A spectrum is formed for each example by taking the ratio of the peak fluxes in each channel between the bounding times (see text). The average spectrum shows the mean of the ratios of each frequency channel, with error bars showing the standard error of the mean.

approximately constant offset following the peak. By defining the bounding UT of the Type III burst as well as its frequency limits following visual examination of the relevant dynamic spectrogram, we can track the peak flux of the Type III burst for each set of fluxes and produce a spectrum of the ratio $\frac{S_Z}{S_{T-III}}$, where S_Z is the flux from equation A1 and S_{T-III} is the flux from the Type III GP inversion with Wind. The example in figure A1 shows the entire Wind/WAVES RAD1 spectrum, including the lower frequencies that the Type III emission does not reach and showing the discrepancy between the two data below $\sim 70{-}100$ kHz. By compiling the spectra of $\frac{S_Z}{S_{T-III}}$ for multiple Type III bursts selected in this way, we can derive an average cross-calibration spectrum with which to scale AKR fluxes from equation 2, giving a better representation of the true intensity of the radio source and allowing a proper comparison between Wind/WAVES fluxes here and those from Cassini/RPWS.

Figure A2 shows the mean $\frac{S_Z}{S_{T-III}}$ spectrum from a set of 19 Type III bursts. The uncertainties on the cross-calibration spectrum are given by the standard error of the mean, and show the better-constrained values at frequencies > 50 kHz for which the majority of the selected Type III bursts are emitting. $\frac{S_Z}{S_{T-III}}$ tends to increase at the lowest frequencies, with the most pronounced increase seen at 20 kHz. This is likely due to the inclusion of spurious emission from the visual examination, as well as the limited num-

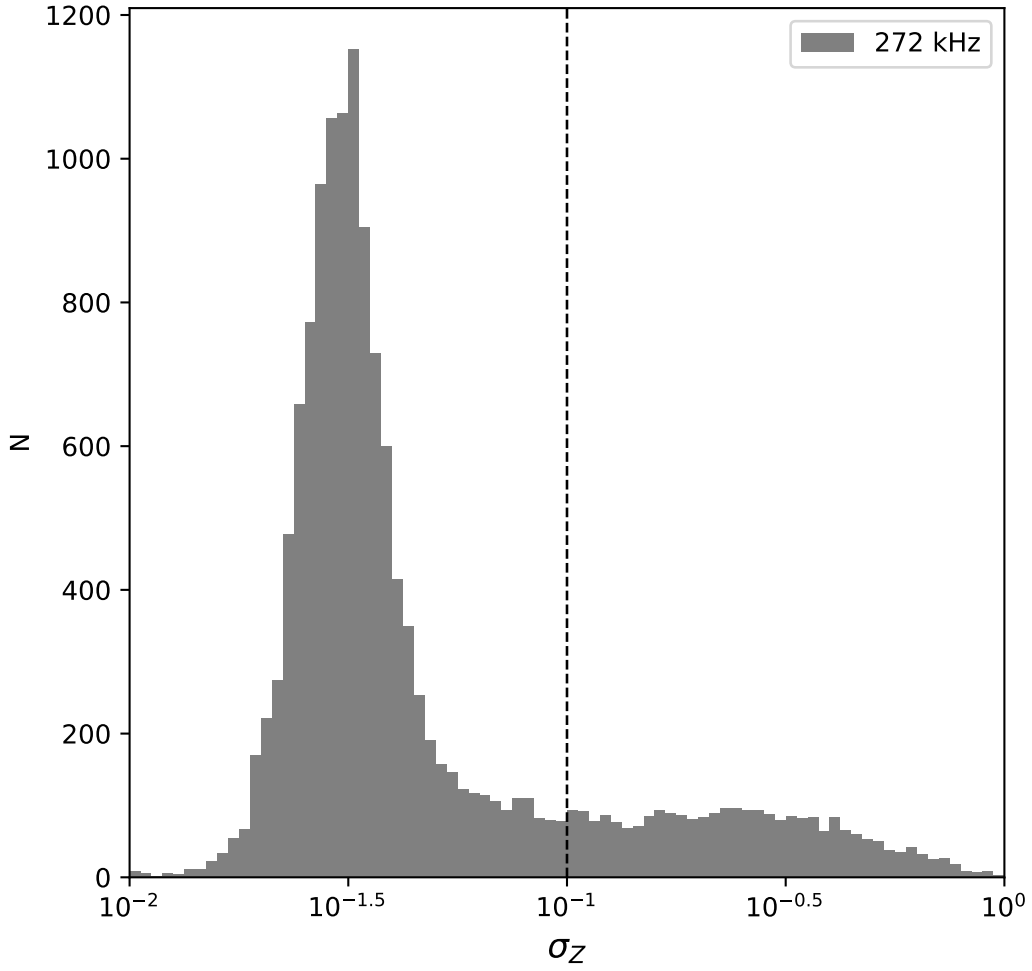

Figure B1. Distribution of σ_Z values for all observations made at 272 kHz during the 30 day period studied here. The black, vertical dashed line shows the value of the threshold ($\sigma_Z \geq 0.1$) chosen to select AKR data.

ber of Type III bursts (7) that were emitting at this frequency. The pre-calibrated flux from equation 2 is multiplied by the cross-calibration spectrum in figure A2 with the exception of the 20 kHz observations which are unmodified.

Appendix B σ_Z Threshold Justification

Figure B1 shows the distribution of σ_Z values observed at 272 kHz and during the 30 day period studied here. This frequency channel was chosen to present as it is a good representation of the typical peak frequency of the AKR spectrum. Shown in the plot is the value used to select AKR data as described in section 2.3; at values lower than this the majority of the emission is found, with a strong Gaussian profile centred roughly on $10^{-1.5}$ representing the majority of other emission such as Type III bursts and background sources, while at values higher than 10^{-1} a second population is seen that contains AKR as well as low frequency contaminants. While determining the exact threshold at which all AKR data is out of the scope of this study, examinations of this metric at other frequencies exhibit similar distributions that lend weight to this choice of the threshold.

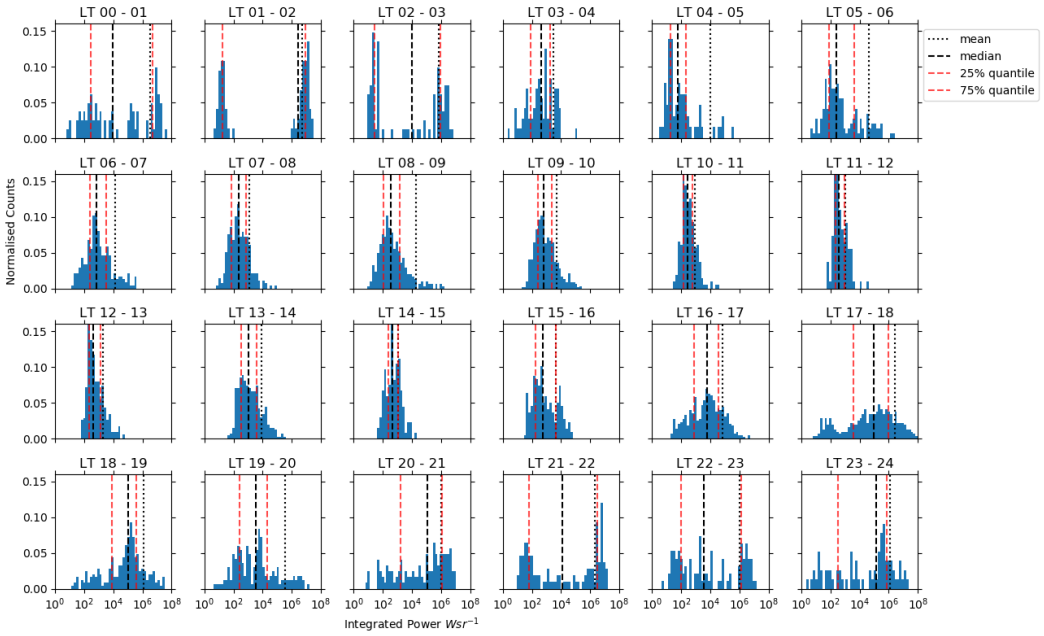

Figure C1. Normalised histograms showing the distribution of log integrated power in each 1 hour LT bin used to create figure 7. Each histogram has black dashed and red dashed vertical lines to represent the median and lower and upper quartiles of the distributions, while the black dotted line shows the mean.

Appendix C AKR Power Distributions with Spacecraft LT

Figure C1 shows the distribution of integrated power observations (100-650 kHz) for each LT bin used to compute the average values for figure 7. From the top and bottom rows, corresponding mostly to LT sectors that Wind travelled through on two, seperate occasions, evidence can be seen that suggests that the distributions are comprised of two seperate events of AKR emission which differ in intensity, whether due to intrinsic differences due to the current state of the magnetosphere or other effects. Some of the bins exhibit two distributions that are seperated by 6 orders of magnitude in some cases (eg 01-02 LT), as well as non-Gaussian distributions (eg 08-09 LT). Applying the selection technique over a longer period will remove some of these local effects and better characterise the statistical AKR power distribution with LT. Taking the mean of the distributions here gives an average that is skewed towards higher values and represents more closely the larger extreme of the total distribution of data, as seen by its position with respect to the 75% quantile in most panels of figure C1. The median of these distributions would be a more statistically rigorous measure of the average. Here, however, where the aim is to demonstrate the empirical selection of AKR data and not to rigorously define the average AKR power of these observations with LT, the mean is sufficient.

Acknowledgments

J. E. W.'s work was supported by the EPSRC Centre for Doctoral Training in Next Generation Computational Modelling Grant No. EP/L015382/1. C. M. J.'s work is supported by the Science Foundation Ireland Grant 18/FRL/6199. D. K. W was supported by the Natural Environment Research Council of the UK under grant NE/S015167/1. The authors acknowledge CNES (Centre National d'Etudes Spatiales), CNRS (Centre National

de la Recherche Scientifique), and Observatoire de Paris for support to the Wind/Waves team and the CDPP (Centre de Données de la Physique des Plasmas) for the provision of the Wind/Waves RAD1 L2 data. We acknowledge support from Paris Astronomical Data Centre (PADC) for the preparation and distribution of the data collection. The Cassini RPWS data from the GP inversion during the period studied here are included in Lamy et al. (2010) and can be found online (`https://doi.org/10.25935/5JFX-DH49` (Cecconi et al., 2017)). The data used in this paper can be found online (`https://doi.org/10.25935/wxv0-vr90`), as can the code used to calibrate and apply the AKR selection (`https://github.com/WatersJE/WindWaves_AKR_calibration_selection`).

References

Akasofu, S. I. (1964). The development of the auroral substorm. *Planetary and Space Science*, *12*(4), 273–282. doi: 10.1016/0032-0633(64)90151-5

Alexander, J. K., & Kaiser, M. L. (1976, dec). Terrestrial kilometric radiation, 1. Spatial structure studies. *Journal of Geophysical Research*, *81*(34), 5948–5956. Retrieved from `http://doi.wiley.com/10.1029/JA081i034p05948` doi: 10.1029/JA081i034p05948

Anderson, R. R., Matsumoto, H., Hashimoto, K., Kojima, H., Kasaba, Y., Kaiser, M. L., ... Rostoker, G. (2005). Geotail, Polar, and Wind Observations of Auroral Kilometric Radiation. *COSPAR Colloquia Series*, *16*(C), 205–219. doi: 10.1016/S0964-2749(05)80032-0

Bougeret, J. L., Kaiser, M. L., Kellogg, P. J., Manning, R., Goetz, K., Monson, S. J., ... Hoang, S. (1995, feb). WAVES: The radio and plasma wave investigation on the wind spacecraft. *Space Sci. Rev.*, *71*(1-4), 231–263. Retrieved from `http://link.springer.com/10.1007/BF00751331` doi: 10.1007/BF00751331

Cane, H. V. (1979, dec). Spectra of the non-thermal radio radiation from the galactic polar regions. *Monthly Notices of the Royal Astronomical Society*, *189*(3), 465–478. Retrieved from `https://ui.adsabs.harvard.edu/abs/1979MNRAS.189..465C/abstracthttps://academic.oup.com/mnras/article-lookup/doi/10.1093/mnras/189.3.465`

Cecconi, B. (2019). Polarization in Low Frequency Radio Astronomy. *arXiv:1901.03599*, 1–26. Retrieved from `http://arxiv.org/abs/1901.03599`

Cecconi, B., Lamy, L., & Zarka, P. (2017). Cassini/rpws/hfr lesia/kronos n3d data collection (version 1.0) [data set]. *PADC*. doi: 10.25935/5JFX-DH49

Dulk, G. A., Erickson, W. C., Manning, R., & Bougeret, J.-L. (2001). Calibration of low-frequency radio telescopes using the galactic background radiation. *Astronomy & Astrophysics*, *365*(2), 294–300.

Gallagher, D. L., & Gurnett, D. A. (1979). Auroral Kilometric Radiation: Time-Averaged Source Location. *Journal of Geophysical Research*, *84*(A11), 6501–6509. doi: 10.1029/JA084iA11p06501

Green, J. L. (2004). Seasonal and solar cycle dynamics of the auroral kilometric radiation source region. *Journal of Geophysical Research*, *109*(A5), A05223. Retrieved from `http://doi.wiley.com/10.1029/2003JA010311` doi: 10.1029/2003JA010311

Green, J. L., Gurnett, D. A., & Shawhan, S. D. (1977, may). The angular distribution of auroral kilometric radiation. *Journal of Geophysical Research*, *82*(13), 1825–1838. Retrieved from `http://doi.wiley.com/10.1029/JA082i013p01825` doi: 10.1029/JA082i013p01825

Gurnett, D. A. (1974, oct). The Earth as a radio source: Terrestrial kilometric radiation. *Journal of Geophysical Research*, *79*(28), 4227–4238. Retrieved from `http://doi.wiley.com/10.1029/JA079i028p04227` doi: 10.1029/JA079i028p04227

Hanasz, J., Panchenko, M., De Feraudy, H., Schreiber, R., & Mogilevsky, M. M. (2003). Occurrence distributions of the auroral kilometric radiation ordinary and extraordinary wave modes. *Journal of Geophysical Research: Space Physics*, *108*(A11). doi: 10.1029/2002JA009579

Hillan, D. S., Cairns, I. H., Robinson, P. A., & Mohamed, A. (2010). Prediction of background levels for the Wind WAVES instrument and implications for the galactic background radiation. *Journal of Geophysical Research: Space Physics*, *115*(A6), 1–11.

Juusola, L., Østgaard, N., Tanskanen, E., Partamies, N., & Snekvik, K. (2011, oct). Earthward plasma sheet flows during substorm phases. *Journal of Geophysical Research: Space Physics*, *116*(A10), n/a–n/a. Retrieved from `http://doi.wiley.com/10.1029/2011JA016852` doi: 10.1029/2011JA016852

Kaiser, M. L., & Alexander, J. K. (1977). Terrestrial Kilometric Radiation III. Average Spectral Properties. , *82*(22).

Kaiser, M. L., Alexander, J. K., Riddle, A. C., Pearce, J. B., & Warwick, J. W. (1978, oct). Direct measurements by Voyagers 1 and 2 of the polarization of terrestrial kilometric radiation. *Geophysical Research Letters*, *5*(10), 857–860. Retrieved from `http://doi.wiley.com/10.1029/GL005i010p00857` doi: 10.1029/GL005i010p00857

Kasaba, Y., Matsumoto, H., Hashimoto, K., & Anderson, R. R. (1997, oct). The angular distribution of auroral kilometric radiation observed by the GEOTAIL spacecraft. *Geophysical Research Letters*, *24*(20), 2483–2486. Retrieved from `http://doi.wiley.com/10.1029/97GL02599` doi: 10.1029/97GL02599

Kepko, L., McPherron, R. L., Amm, O., Apatenkov, S., Baumjohann, W., Birn, J., ... Sergeev, V. (2015). Substorm Current Wedge Revisited. *Space Science Reviews*, *190*(1-4), 1–46. Retrieved from `http://dx.doi.org/10.1007/s11214-014-0124-9` doi: 10.1007/s11214-014-0124-9

Kimura, T., Lamy, L., Tao, C., Badman, S. V., Kasahara, S., Cecconi, B., ... Fujimoto, M. (2013). Long-term modulations of Saturn's auroral radio emissions by the solar wind and seasonal variations controlled by the solar ultraviolet flux. *Journal of Geophysical Research: Space Physics*, *118*(11), 7019–7035. doi: 10.1002/2013JA018833

Krupar, V., Maksimovic, M., Kontar, E. P., Zaslavsky, A., Santolik, O., Soucek, J., ... Szabo, A. (2018). Interplanetary Type III Bursts and Electron Density Fluctuations in the Solar Wind. *The Astrophysical Journal*, *857*(2), 82. Retrieved from `http://dx.doi.org/10.3847/1538-4357/aab60f` doi: 10.3847/1538-4357/aab60f

Lamy, L., Zarka, P., Cecconi, B., Hess, S., & Prangé, R. (2008). Modeling of Saturn kilometric radiation arcs and equatorial shadow zone. *Journal of Geophysical Research: Space Physics*, *113*(10), 1–10. doi: 10.1029/2008JA013464

Lamy, L., Zarka, P., Cecconi, B., & Prangé, R. (2010, sep). Auroral kilometric radiation diurnal, semidiurnal, and shorter-term modulations disentangled by Cassini. *Journal of Geophysical Research: Space Physics*, *115*(A9), n/a–n/a. Retrieved from `http://doi.wiley.com/10.1029/2010JA015434` doi: 10.1029/2010JA015434

Lamy, L., Zarka, P., Cecconi, B., Prangé, R., Kurth, W. S., & Gurnett, D. A. (2008, jul). Saturn kilometric radiation: Average and statistical properties. *Journal of Geophysical Research: Space Physics*, *113*(A7), n/a–n/a. Retrieved from `http://doi.wiley.com/10.1029/2007JA012900` doi: 10.1029/2007JA012900

Liou, K. (2002). Magnetic dipolarization with substorm expansion onset. *Journal of Geophysical Research*, *107*(A7), 1131. Retrieved from `http://doi.wiley.com/10.1029/2001JA000179` doi: 10.1029/2001JA000179

Liou, K., Meng, C.-I., Lui, A. T. Y., Newell, P. T., & Anderson, R. R. (2000, nov). Auroral kilometric radiation at substorm onset. *Journal of Geophysical Re-*

search: Space Physics, *105*(A11), 25325–25331. Retrieved from http://doi.wiley.com/10.1029/2000JA000038 doi: 10.1029/2000JA000038

Manning, R., & Dulk, G. A. (2001). The Galactic background radiation from 0.2 to 13.8 MHz. *Astronomy & Astrophysics*, *372*(2), 663–666.

Manning, R., & Fainberg, J. (1980). A New Method of Measuring Radio Source Parameters of a Partially Polarized Distributed Source from Spacecraft Observations. *Space Sci. Instrum.*, *5*, 161–181.

McPherron, R. L., Russell, C. T., & Aubry, M. P. (1973). Satellite studies of magnetospheric substorms on August 15, 1968: 9. Phenomenological model for substorms. *Journal of Geophysical Research*, *78*(16), 3131–3149. doi: 10.1029/ja078i016p03131

Meyer-Vernet, N., Hoang, S., Issautier, K., Maksimovic, M., Manning, R., Moncuquet, M., & Stone, R. G. (n.d.). Measuring plasma parameters with thermal noise spectroscopy.

Meyer-Vernet, N., Issautier, K., & Moncuquet, M. (2017). Quasi-thermal noise spectroscopy: The art and the practice. *Journal of Geophysical Research: Space Physics*, *122*(8), 7925–7945. doi: 10.1002/2017JA024449

Meyer-Vernet, N., & Perche, C. (1989). Tool kit for antennae and thermal noise near the plasma frequency. *Journal of Geophysical Research*, *94*(A3), 2405. Retrieved from http://doi.wiley.com/10.1029/JA094iA03p02405 doi: 10.1029/JA094iA03p02405

Morioka, A., Miyoshi, Y., Kurita, S., Kasaba, Y., Angelopoulos, V., Misawa, H., ... McFadden, J. P. (2013). Universal time control of AKR: Earth is a spin-modulated variable radio source. *Journal of Geophysical Research: Space Physics*, *118*(3), 1123–1131. doi: 10.1002/jgra.50180

Morioka, A., Miyoshi, Y., Tsuchiya, F., Misawa, H., Kasaba, Y., Asozu, T., ... Reinisch, B. W. (2011). On the simultaneity of substorm onset between two hemispheres. *Journal of Geophysical Research: Space Physics*, *116*(4). doi: 10.1029/2010JA016174

Morioka, A., Miyoshi, Y., Tsuchiya, F., Misawa, H., Sakanoi, T., Yumoto, K., ... Donovan, E. F. (2007). Dual structure of auroral acceleration regions at substorm onsets as derived from auroral kilometric radiation spectra. *Journal of Geophysical Research: Space Physics*, *112*(6), 1–13. doi: 10.1029/2006JA012186

Mutel, R. L., Christopher, I. W., & Pickett, J. S. (2008). Cluster multispacecraft determination of AKR angular beaming. *Geophysical Research Letters*, *35*(7), 1–6. doi: 10.1029/2008GL033377

Mutel, R. L., Gumett, D. A., Christopher, I. W., Pickett, J. S., & Schlax, M. (2003). Locations of auroral kilometric radiation bursts inferred from multispacecraft wideband Cluster VLBI observations. 1: Description of technique and initial results. *Journal of Geophysical Research: Space Physics*, *108*(A11), 1–13. doi: 10.1029/2003JA010011

Mutel, R. L., Gurnett, D. A., & Christopher, I. W. (2004). Spatial and temporal properties of AKR burst emission derived from Cluster WBD VLBI studies. *Annales Geophysicae*, *22*(7), 2625–2632. doi: 10.5194/angeo-22-2625-2004

Novaco, J. C., & Brown, L. W. (1978, apr). Nonthermal galactic emission below 10 megahertz. *The Astrophysical Journal*, *221*(A6), 114. Retrieved from http://adsabs.harvard.edu/doi/10.1086/156009 doi: 10.1086/156009

Panchenko, M. (2003, dec). Direction finding of AKR sources with three orthogonal antennas. *Radio Science*, *38*(6), n/a–n/a. Retrieved from http://doi.wiley.com/10.1029/2003RS002929 doi: 10.1029/2003RS002929

Panchenko, M., Khodachenko, M. L., Kislyakov, A. G., Rucker, H. O., Hanasz, J., Kaiser, M. L., ... Goetz, K. (2009). Daily variations of auroral kilometric radiation observed by STEREO. *Geophysical Research Letters*, *36*(6), 2–5.

Pulupa, M., Bale, S. D., Badman, S. T., Bonnell, J. W., Case, A. W., de Wit, T. D.,

... Whittlesey, P. (2019). Statistics and Polarization of Type III Radio Bursts Observed in the Inner Heliosphere. *The Astrophysical Journal Supplement Series*, *246*(2), 49. Retrieved from http://arxiv.org/abs/1912.03371{\%}0A doi: 10.3847/1538-4365/ab5dc0

Reiner, M. J., Fainberg, J., Kaiser, M. L., & Bougeret, J. L. (2007). Circular polarization observed in interplanetary type III radio storms. *Solar Physics*, *241*(2), 351–370. doi: 10.1007/s11207-007-0277-8

Schreiber, R., Panchenko, M., Hanasz, J., Mutel, R., & Christopher, I. (2017). Beaming of intense AKR seen from the Interball-2 spacecraft. *Journal of Geophysical Research: Space Physics*, *122*(1), 249–257. doi: 10.1002/2015JA022197

Shue, J.-H., Song, P., Russell, C. T., Steinberg, J. T., Chao, J. K., Zastenker, G., ... Kawano, H. (1998). Magnetopause location under extreme solar wind conditions. *Journal of Geophysical Research: Space Physics*, *103*(A8), 17691–17700. doi: 10.1029/98ja01103

Voots, G. R., Gurnett, D. A., & Akasofu, S. I. (1977, jun). Auroral kilometric radiation as an indicator of auroral magnetic disturbances. *Journal of Geophysical Research*, *82*(16), 2259–2266. Retrieved from http://doi.wiley.com/10.1029/JA082i016p02259 doi: 10.1029/JA082i016p02259

Wu, C. S., & Lee, L. C. (1979). A theory of the terrestrial kilometric radiation. *The Astrophysical Journal*, *230*, 621. Retrieved from http://adsabs.harvard.edu/doi/10.1086/157120 doi: 10.1086/157120

Wu, D. J., Chao, J. K., & Lepping, R. P. (2000, jun). Interaction between an interplanetary magnetic cloud and the Earth's magnetosphere: Motions of the bow shock. *Journal of Geophysical Research: Space Physics*, *105*(A6), 12627–12638. Retrieved from http://doi.wiley.com/10.1029/1999JA000265 doi: 10.1029/1999JA000265

Zarka, P., Cecconi, B., & Kurth, W. S. (2004). Jupiter's low-frequency radio spectrum from Cassini/Radio and Plasma Wave Science (RPWS) absolute flux density measurements. *Journal of Geophysical Research: Space Physics*, *109*(A9), 1–18.

Zaslavsky, A., Meyer-Vernet, N., Hoang, S., Maksimovic, M., & Bale, S. D. (2011). On the antenna calibration of space radio instruments using the galactic background: General formulas and application to STEREO/WAVES. *Radio Science*, *46*(2), 1–7. doi: 10.1029/2010RS004464

Zhao, W., Liu, S., Zhang, S., Zhou, Q., Yang, C., He, Y., ... Xiao, F. (2019). Global Occurrences of Auroral Kilometric Radiation Related to Suprathermal Electrons in Radiation Belts. *Geophysical Research Letters*, *2*, 7230–7236. doi: 10.1029/2019GL083944